Climate change has intensified exceptional El Niño events like the 2026/27 forecast

Aditya Sengupta[1,2], Mandy B. Freund[1,2] and Andrew D. King[1,2]

[1]School of Geography, Earth and Atmospheric Sciences, University of Melbourne, Melbourne, Kulin nations, Australia
[2]ARC Centre of Excellence for Weather of the 21st Century, Australia

E-mail: aditya.sengupta@student.unimelb.edu.au

Keywords: El Niño; extreme event attribution; seasonal forecasting; CMIP

Abstract
Extreme El Niño events disrupt weather across much of the globe, with adverse effects on agriculture, fisheries and economic output that persist for several years. Event attribution routinely quantifies the human influence on individual heatwaves, droughts and floods, but its application to the El Niño events that drive many of them has been much more limited. Here we investigate the 2026/27 El Niño event, forecast to peak later this year. We assess it using the relative Niño3.4 index, adopted operationally by forecasting agencies, which measures the Niño3.4 anomaly against the concurrent tropical mean. Multimodel forecasts indicate a peak of 3.16 °C, exceeding the largest event in the instrumental record (1982/83) in 84% of ensemble members. Using generalised Pareto fits to pre-industrial and current climate simulations from models evaluated on ENSO asymmetry, we find that an event of this magnitude is approximately six times more likely in the current climate. The 2026/27 forecast exemplifies how climate change is already altering the rarity and intensity of extreme El Niño events.

1 Introduction

There is considerable speculation about the intensifying El Niño event in the Pacific Ocean. El Niño events reshape weather patterns across much of the globe, causing global mean surface temperature to spike (Jiang et al., 2025; Raghuraman et al., 2024). El Niño events have widespread impacts on rainfall, agriculture, fisheries and public health (McPhaden et al., 2006; Winters, 2026). These impacts carry a substantial economic cost, and this cost persists long after the event itself has decayed. Global economic growth was found to be suppressed for years following the 1982/83 and 1997/98 El Niño events, costing the global economy trillions of dollars (Callahan and Mankin, 2023), and these losses are projected to grow as the climate warms (Liu et al., 2023). The strongest events can significantly increase the likelihood of damages; therefore quantifying the frequency of extreme events is essential.

Extreme event attribution has become a standard tool for quantifying the human influence on individual weather events, and is often applied to heatwaves, droughts, floods and fires (Stott et al., 2016; Philip et al., 2020; Otto et al., 2024). But its application to El Niño events themselves has been limited (Herring et al., 2018), despite El Niño being the largest driver of interannual climate variability and the trigger for many of the extremes to which the method is applied. Work on ENSO under warming has instead focused on how the statistical characteristics of extreme El Niño events are projected to change (Cai et al., 2015, 2023; Yeh et al., 2018; Chung et al., 2024), which is a different question from how much more likely a particular event has become. The latter is harder to quantify since the conventional Oceanic Niño Index (ONI), defined as a Niño3.4 anomaly relative to a fixed 30-year climatology, increasingly mixes the ENSO signal with the warming background state (van Oldenborgh et al., 2021a). An event defined in these terms cannot be compared between a pre-industrial and a present-day climate, since the index itself contains the warming being attributed. Since February 2026, NOAA's Climate Prediction Center has monitored El Niño using the relative Oceanic Niño index (RONI), which subtracts the concurrent tropical-mean sea surface temperature (SST) anomaly. The RONI measures how anomalously warm the central-eastern Pacific is relative to the rest of the tropics (L'Heureux et al., 2024b), and other forecasting agencies are also starting to use RONI (Wheeler et al., 2024). Since RONI removes the background warming by construction, it provides a basis on which events in different climates can be compared more directly.

Forecasts initialised in August 2026 indicate an exceptional El Niño developing through the second half of the year. The tropical Pacific was in a weak La Niña state through late 2025, crossed the El Niño threshold during boreal spring 2026, and has warmed steadily since (Readfearn et al., 2026; Luhn, 2026). The amplitude-corrected multimodel ensemble mean peaks at 3.16 °C, with individual forecast members spanning 2.22–3.98 °C (Figure 1b). Here we use the 2026/27 El Niño to carry out attribution analysis of this potentially exceptional individual El Niño event magnitude and to quantify how the likelihood of events of this strength has changed due to human-caused climate change.

2 Data and Methods

2.1 Datasets

We used five monthly SST datasets to characterise observed El Niño events: COBE-SST (Ishii et al., 2025), DCSST-I (Chan et al., 2026, 2025), HadISST (Rayner et al., 2003), ERSSTv5 (Huang et al., 2017) and HadSST4 (Kennedy et al., 2019). We primarily focus on the first four datasets, which are spatially complete, and we used these for all quantitative results. HadSST4 is not infilled, and we present it alongside the other datasets for comparison. All anomalies were computed relative to a 1991–2020 monthly climatology, which is used for operational relative Niño3.4 (RONI) index forecasts (L'Heureux et al., 2024b).

For the 2026/27 forecast, we used the North American multimodel Ensemble (Kirtman, 2016) (NMME) initialised in the month of August 2026, obtained from the Columbia University Center for Climate Systems Research (CCSR) NMME archive. The forecast range in our study is based on 70 ensemble members from four models available in the CCSR NMME archive: NASA-GMAO GEOSS2S, ECCC CanSIPS-IC4, COLA-RSMAS CCSM4 and CESM1. We do not include NCEP-CFSv2 because the hindcasts required for amplitude correction are not provided alongside its forecasts in that archive, although its uncorrected forecast falls within the range of the remaining models. NOAA-GFDL SPEAR had not released its August 2026 forecast at the time of analysis, and is therefore also excluded.

For the attribution analysis, we used monthly surface temperature (ts) data from CMIP5 (Taylor et al., 2012) and CMIP6 (Eyring et al., 2016) models, taking a single realisation per model (r1i1p1 and r1i1p1f1 respectively) from three experiments: piControl, historical, and a moderate-forcing future scenario: RCP4.5 for CMIP5 (Moss et al., 2010) and SSP2-4.5 for CMIP6 (Tebaldi et al., 2021). We used 68 models which had all three experiments available, and for each of these models we concatenated the historical and scenario runs to cover a continuous 1850–2050 time period.

2.2 Relative Niño3.4 index calculation

We computed the RONI following the definition adopted operationally by NOAA's Climate Prediction Center (L'Heureux et al., 2024b; van Oldenborgh et al., 2021a; Wheeler et al., 2024). RONI is the three-month running mean of the Niño3.4 (5°S-5°N, 170°-120°W) SST anomaly minus the concurrent tropical-mean (20°S-20°N) SST anomaly, rescaled so that its variance matches that of the conventional Oceanic Niño Index. In the models, we masked land gridpoints to restrict the tropical mean calculation to the ocean gridpoints only. We identified observed events using the NOAA Climate Prediction Center (CPC) operational criterion of RONI ≥ 0.5 °C for at least five consecutive overlapping three-month seasons, and defined the event magnitude as the peak RONI value within each event. The timing of the event was defined by the calendar year of the peak.

For the forecast, we first computed the anomalies relative to each model's own 1991–2020 hindcast climatology, and then constructed RONI from each ensemble member individually. Coupled forecast models systematically overstate ENSO amplitude at multi-month lead-times (Barnston et al., 2017, 2012; Kumar et al., 2015; Ehsan et al., 2024), so we subsequently applied the amplitude correction used operationally by NOAA CPC (Tippett et al., 2017). This was done by dividing the forecast Niño3.4 anomalies by the ratio of the model's hindcast standard deviation to the observed standard deviation, computed separately for each model's August-initialised hindcasts over 1991–2020. These standard deviations were computed across individual members rather than across ensemble means, so that the correction does not depend on ensemble size, and we constrained the resulting factors to lie between 0.5 and 3.5 to guard against poorly sampled leads. Following this, we took the probability of the 2026/27 forecast event exceeding the observed record as the fraction of amplitude-corrected members in which peak RONI exceeds the observed 1982/83 value, and we report the uncertainty range by using the 1982/83 value in each of the observational datasets.

2.3 Model evaluation and selection

Since the analysis concerns extreme El Niño events, we required models to reproduce the observed asymmetry of ENSO (Bellenger et al., 2013; Planton et al., 2021) before including them in the attribution analysis. To evaluate the models, we first calculated the uncertainty range of RONI skewness using the four infilled observational datasets. For each dataset, the sampling distribution of RONI skewness over 1900–2000 was estimated using a moving-block bootstrap (Künsch, 1989; Politis and Romano, 1994) with 10,000 resamples and 36-month blocks, chosen to preserve individual ENSO events. The 5–95% intervals of the four datasets overlap, indicating that they are statistically consistent, and we took their intersection, [+0.18, +0.44], as the reference skewness range for model evaluation. This range is insensitive to the choice of block length between 24 and 60 months. Eighteen models met our evaluation criteria: eight CMIP6 and ten CMIP5 models (Supplementary Table S1), and the observational datasets fall within the spread of these models in the upper tail (Supplementary Figure S1). We then multiplied each retained model's index by the ratio of the observed to simulated ENSO standard deviation over 1900–2000, applying a single factor per model to all of its experiments, so that absolute thresholds were comparable across models while forced differences between experiments were preserved.

2.4 Attribution analysis

We took piControl as the pre-industrial counterfactual (Diffenbaugh et al., 2017) and the 2000–2050 period of the concatenated historical and future scenario runs as the proxy for the current climate (van Oldenborgh et al., 2021b; Kirchmeier-Young et al., 2019; Otto et al., 2024). RONI indices were calculated in these two periods against the 1991–2020 baseline climatology, taken from each model's own historical and scenario run. We defined event magnitudes as annual block maxima, taking the largest index value in each complete ENSO year (July–June). Annual maxima were pooled across models, with each model contributing at most 500 years, to ensure that models with long piControl runs did not dominate the counterfactual return periods.

The exceedance probabilities were estimated by fitting a generalised Pareto distribution (GPD) to values above the 85th percentile (Coles, 2001). We chose a GPD rather than a generalised extreme value (GEV) distribution fitted to block maxima, since the GEV fit underestimated the piControl tail beyond return periods of about 100 years. The GPD instead reproduced the empirical exceedances out to return periods of 10^4 years, with a shape parameter that is stable between -0.08 and -0.11 across thresholds from the 70th to the 95th percentile (Supplementary Figure S2). The shape parameters fitted independently to the two climates are statistically indistinguishable (difference of -0.12; 90% c.i. of -0.24 to $+0.02$), so we adopted a common shape estimated from the better constrained pre-industrial sample, and allowed only the location and scale to differ between climates.

The likelihood of the event was estimated using the probability ratio defined as the ratio of the exceedance probability of a given magnitude in the current climate to its exceedance probability in the pre-industrial climate (Stott et al., 2016; Philip et al., 2020). The metric of intensity change expresses the same shift along the magnitude axis rather than the probability axis, and describes how much stronger an event of the same rarity has become. To calculate this, we first obtained the exceedance probability of the forecast magnitude in the current climate, and then identified the magnitude with that same exceedance probability in the pre-industrial climate, and took the difference between the two. All uncertainty ranges presented here are 90% confidence intervals (5–95% percentiles) from a bootstrap that resamples whole models with replacement over 1000 iterations, since structural differences between models dominate sampling uncertainty.

2.5 Sensitivity tests

We repeated the attribution under a range of analytical choices to assess robustness. We varied the GPD threshold between the 75th and 90th percentiles, fitted the two climates with independently estimated shape parameters, fitted a GEV to block maxima in place of a GPD, restricted the ensemble to each model generation in turn, excluded the models requiring the largest amplitude corrections, and omitted each model in turn. Results of these tests are given in Supplementary Table S3.

We also computed trends in relative Niño3.4 SST in both models and observations (see Supplementary Table S4). For each observational dataset and each model, we calculated the annual-mean difference between the Niño3.4 and the ocean-masked tropical-mean SST, and fitted a linear trend over three periods: 1900–2025, 1950–2025 and 1980–2025. For the models, these time series were taken from the concatenated historical and scenario runs.

3 Results

We find that the peak amplitude of this event would exceed the strongest El Niño in the instrumental record. Since 1870, the largest observed peak RONI is that of the 1982/83 event, on average at 2.65 °C across the four infilled datasets, followed by the 1877/78 (2.58), 1888/89 (2.55), 2015/16 (2.48) and 1997/98 (2.42) events (Figure 1a). The amplitude-corrected forecast for 2026/27 exceeds all of these, and 84% of the individual forecast members peak above the 1982/83 value. The observed record is itself uncertain, since the four datasets disagree on the magnitude of the 1982/83 peak by 0.27 °C (2.55–2.82 °C), and taking each dataset in turn as the reference gives an exceedance probability of between 81% and 87%. We note that this comparison is made in RONI, from which the concurrent tropical-mean warming has already been removed. Even on longer timescales, palaeoclimate reconstructions suggest that no El Niño event since at least 1600 CE exceeded the forecast peak magnitude for the current event (Freund et al., 2019). The forecast event is therefore exceptional due to the warming in central-eastern equatorial Pacific compared to rest of the tropics, which is the quantity that governs the atmospheric response to warmer sea surface temperature (SST) (Johnson and Xie, 2010; Izumo et al., 2020).

The forecast SST pattern also exceeds all previous observations across most locations within the central and eastern equatorial Pacific. We compared the forecast December–February relative SST with the highest value observed at each gridpoint in any December–February since 1870, and found that the forecast exceeds the observed maximum over roughly 70% of the Niño3.4 region and nearly 20% of the tropical Pacific (15°S–15°N, 140°E–80°W; Figure 1c).

We find that an event of the 2026/27 forecast magnitude is about six times more likely than it would have been in a pre-industrial climate using an ensemble of 18 climate models evaluated against the observed asymmetry of ENSO (see Extended Data Fig. S1 and Extended Data Table S1). An event of this magnitude occurs roughly once in 1500 years in the pre-industrial simulations, and roughly once in 240 years in the current climate, giving a probability ratio of 6.2 (3.1–15.2 90% confidence interval; Supplementary Table S2). We also find that the forecast event is 0.61 °C stronger than a comparably rare event in the pre-industrial climate.

The change in the mean state accounts for roughly two-thirds of the increase in likelihood, while the increase in variability accounts for the remaining third. Since the fitted distributions share a

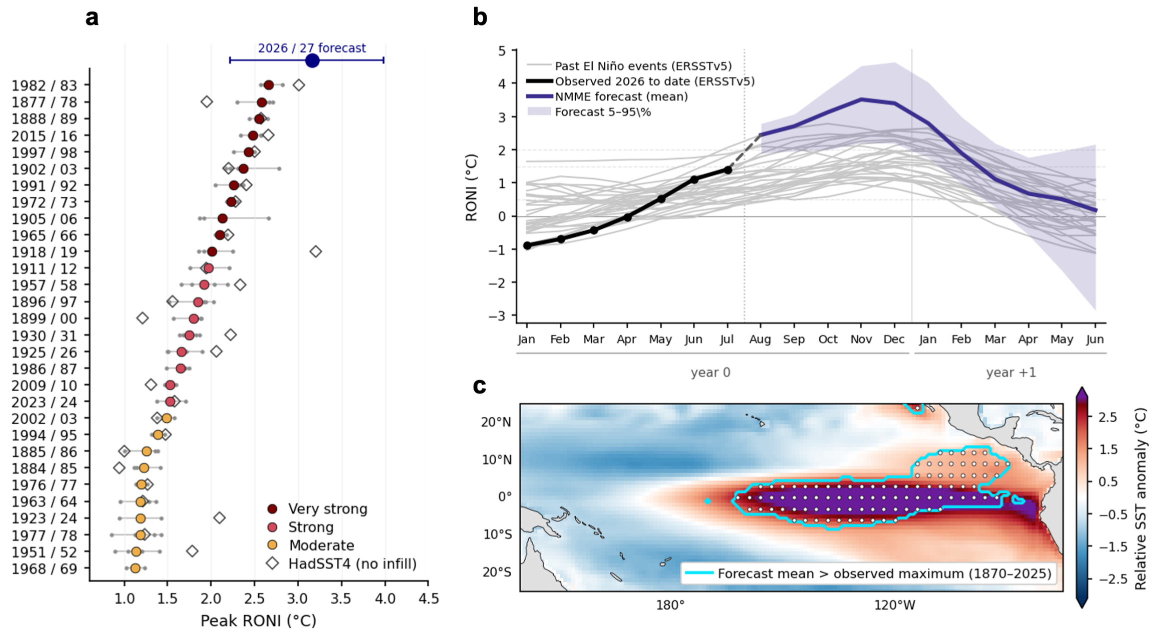

Figure 1. The forecast 2026/27 El Niño in the context of the observed instrumental record. **a**, Peak RONI of every observed moderate to very-strong El Niño event since 1870, ranked by magnitude. Coloured circles show the mean across the four infilled SST analyses, grey dots highlight the individual datasets and grey bars highlight their range; open diamonds show HadSST4, which is not infilled so is not directly comparable. Circle colour denotes event category (moderate, strong and very strong). The purple marker at the top shows the amplitude-corrected multimodel forecast for 2026/27 initialised in August 2026, with the bar spanning the 5th–95th percentile of forecast members. **b**, RONI evolution of each moderate to very-strong El Niño event from January of the event year to June of the following year. Grey lines show all observed events since 1870 in ERSSTv5, the black line with markers shows observations to date for 2026, and the purple line shows the mean of the amplitude-corrected NMME forecast initialised in August 2026, with shading spanning the 5th–95th percentile across members. The dotted vertical line marks the forecast initialisation. **c**, Forecast relative SST anomaly for December–February 2026/27, averaged across the four NMME models. Cyan contours and white stippling mark gridpoints where the forecast mean exceeds the highest value observed at that location in any December–February since 1870.

common shape parameter, they differ only in location and scale and so the two contributions can be separated. The threshold shifts by +0.44°C between the two climates and the scale increases by a factor of 1.109. Holding the scale fixed and applying only the shift gives a probability ratio of 3.9, while holding the location fixed and applying only the change in scale gives 1.9, against 6.2 for the two combined. The shift in the distribution, which represents a change in the mean state, therefore accounts for roughly two-thirds of the increase in likelihood, and the increase in variability accounts for the remaining third. The two contributions are simulated differently across the model generations: the Niño3.4 region warms faster than the tropical mean in 16 of the 18 models, by +0.16°C on average in the underlying SST, whereas the increase in variability is largely confined to the CMIP6 models (mean ratio of 1.33, against 1.00 for CMIP5; see Supplementary Figure S3) (Cai et al., 2023, 2015; Maher et al., 2023; Yeh et al., 2018).

We repeated the attribution under a range of analytical choices to assess robustness (Supplementary Table S3). The probability ratio for the forecast magnitude is insensitive to the GPD threshold, varying between 6.1 and 7.7 for thresholds from the 75th to the 90th percentile. It is also insensitive to the exclusion of the models requiring the largest amplitude corrections (5.1). Omitting each model in turn gives ratios in the range of 5.1 and 9.2. Restricting the ensemble to either model generation leaves the central estimate within the range of the full ensemble, at 6.4 for CMIP6 alone and 5.0 for CMIP5 alone, although the confidence intervals of the two subsets are correspondingly wider and overlap substantially. Fitting the two climates with independently estimated shape parameters, rather than a common shape parameter, gives a probability ratio of 4.2. Fitting a GEV to block maxima, instead of GPD, gives a ratio of 17.3. Both alternatives are

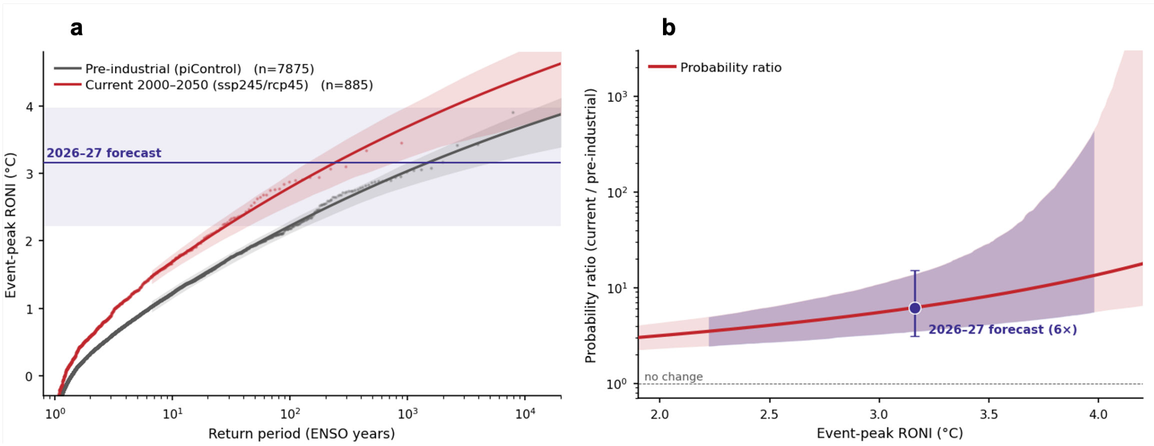

Figure 2. Attribution of extreme El Niño likelihood to anthropogenic warming. **a**, Return levels of annual peak RONI in the pre-industrial climate (piControl, grey) and the current climate (2000–2050 of historical + RCP4.5/SSP2-4.5, red), pooled across 18 evaluated CMIP models. Dots show empirical annual maxima, solid lines show the common-shape generalised Pareto fits, and shading highlights the 5th–95th percentile range from a bootstrap resampling across models. The horizontal purple line and shading show the forecast 2026/27 magnitude and its 5th–95th percentile range across forecast members. **b**, Probability ratio between the current and pre-industrial climates as a function of event magnitude. The red line shows the central estimate and red shading highlights the bootstrap 5th–95th percentile range; the purple shaded region highlights the same range over the magnitudes spanned by the forecast uncertainty. The purple marker shows the central estimate of the forecast magnitude, and vertical bars show the bootstrap range on the probability ratio for the central estimate. The dashed line marks a probability ratio of one, indicating no change in likelihood.

less well constrained at this magnitude of RONI. The independent shape parameter fit causes the two distributions to converge in the upper tail, while the GEV fit underestimates the pre-industrial tail, as described in the methods section.

Since the mean-state warming in the Niño3.4 region is a larger contribution to the likelihood estimate compared to variability change, we assess whether this change is evident in observations. Our attribution rests on the difference between the pre-industrial and current climates simulated by each model rather than on the historical trend, but as a consistency check, we compared trends in relative Niño3.4 SST between models and observations (Supplementary Table S4). All four observational datasets give negative trends over the three periods, indicating that the Niño3.4 region has warmed more slowly than the tropical mean, and these trends become more negative over the more recent periods. The models give a multimodel mean of between +0.12 and +0.15 °C per century, with 13 to 16 of the 18 models showing a positive trend, although only three are significant at the 5% level in any period. This difference between observed and simulated SST trend patterns in the tropical Pacific is well documented, and it remains unresolved whether it reflects a common model bias, internal variability in the observed record, or a combination of the two (Lee et al., 2022; Watanabe et al., 2024). Each model here contributes a single realisation, so the simulated spread does not fully sample internal variability and the apparent separation from the observations is correspondingly overstated. To test how much this matters, we recomputed the attribution retaining only the increase in ENSO variability and discarding the mean-state contribution entirely, which gives a probability ratio of about two. The discrepancy therefore affects the size of the estimated change in likelihood, but not its sign, nor the conclusion that an event of this magnitude has become substantially more likely.

4 Discussion and Conclusions

Some aspects limit our analysis. Each model contributes a single realisation, so the spread across the ensemble reflects structural differences and internal variability together, and the model bootstrap samples both. The forecast magnitude lies beyond the range of the pooled current-climate maxima, so the probability ratio at this magnitude depends on the fitted tail rather than on the empirical distribution; the sensitivity tests indicate that this dependence is modest for the GPD fit but substantial if a GEV fit is used instead. The evaluation step also selects models on ENSO asymmetry alone, and a model that reproduces the observed skewness need not reproduce the observed response of ENSO to forcing.

Despite these caveats, the direction and approximate size of the change are robust. Every sensitivity test gives a probability ratio above one, and the majority fall between 4 and 9. The most conservative treatment, in which the mean-state contribution is set aside entirely and only the increase in ENSO variability is retained, still gives a doubling of the likelihood. An event of the magnitude now forecast is therefore substantially more likely in the current climate than in a pre-industrial climate. While, our conclusions about the 2026/27 event therefore remain conditional on the forecast being accurate, the attribution result does not depend on the accuracy of a forecast, since it concerns events of a given magnitude rather than this particular event.

Extreme El Niño events have large economic and societal impacts, and if the 2026/27 forecast eventuates it will probably be an unprecedented event. An El Niño of this magnitude is now substantially more likely than it would have been in a pre-industrial climate, and will become more likely still as the world continues to warm. Attribution of this kind has, until now, largely been carried out for the weather extremes that El Niño events can exacerbate, rather than for the events themselves. More intense El Niño events also have a stronger control over global and regional climate anomalies (L'Heureux et al., 2024a) which will be enhanced in warming climate (Liu et al., 2026).

As humanity continues to emit greenhouse gases into the atmosphere, the intensity, and frequency of future El Niño events that would once have been considered exceptional could increase further. As the tropical background continues to warm, the difference between absolute and relative measures of ENSO will widen further (van Oldenborgh et al., 2021a; Wheeler et al., 2024), and monitoring events in relative terms will become even more important in the future (Wheeler et al., 2024; L'Heureux et al., 2024b). Therefore, our findings call for adaptation planning built around a shifting baseline of ENSO risk rather than a historical one, and for rapid reductions in CO_2 emissions to prevent that baseline from shifting further.

Acknowledgments

The PhD research of AS is supported by the University of Melbourne through the Melbourne Research Scholarship and John and Allan Gilmour Research Award (Science). AS, ADK and MBF also receive funding from the ARC Centre of Excellence for the Weather of the 21st Century (CE230100012). ADK also receives funding from an ARC Future Fellowship (FT240100306). This research was undertaken with data supported by the Australian Government's National Collaborative Research Infrastructure Strategy (NCRIS), with access to resources provided through the ACCESS-NRI Merit Allocation Scheme and the National Computational Infrastructure (NCI).

Declaration

The authors would like to declare no competing interests

Author contributions

AS: Conceptualization, Formal analysis, Methodology, Visualization, Writing - original draft, Writing - review and editing;
MBF: Supervision, Methodology, Visualization, Writing - review and editing;
ADK: Supervision, Methodology, Visualization, Writing - review and editing

Data availability

All datasets used in this study are publicly available. The observational SST datasets were obtained from their respective providers: COBE-SST from the Japan Meteorological Agency and NOAA Physical Sciences Laboratory (https://psl.noaa.gov/data/gridded/data.cobe.html), ERSSTv5 from NOAA NCEI (https://www.ncei.noaa.gov/products/extended-reconstructed-sst), HadISST (https://www.metoffice.gov.uk/hadobs/hadisst/) and HadSST4 (https://www.metoffice.gov.uk/hadobs/hadsst4/) from the Met Office Hadley Centre, and DCSST-I from Harvard Dataverse (https://doi.org/10.7910/DVN/NU4UGW). The operational relative Niño3.4 index and its documentation are available from NOAA's Climate Prediction Center (https://www.cpc.ncep.noaa.gov/products/analysis_monitoring/enso/roni/). The North American Multimodel Ensemble forecasts and hindcasts were obtained from the Columbia University/CCSR NMME archive (https://forecast.ccsr.columbia.edu/data/NMME/). CMIP5 and CMIP6 model output is available through the Earth System Grid Federation (https://esgf.llnl.gov/), and was accessed here through the replica collections hosted by the National Computational Infrastructure (NCI) Australia. The code required to reproduce the figures and the results of this study is available at https://github.com/adisen99/extreme_el_nino_2026, archived on Zenodo at https://doi.org/10.5281/zenodo.21931339.

References

Barnston, A. G., Tippett, M. K., L'Heureux, M. L., Li, S., and DeWitt, D. G. (2012). Skill of Real-Time Seasonal ENSO Model Predictions During 2002–11: Is Our Capability Increasing?

Barnston, A. G., Tippett, M. K., Ranganathan, M., and L'Heureux, M. L. (2017). Deterministic skill of ENSO predictions from the North American Multimodel Ensemble. *Climate Dynamics*, 53(12):7215–7234.

Bellenger, H., Guilyardi, E., Leloup, J., Lengaigne, M., and Vialard, J. (2013). ENSO representation in climate models: from CMIP3 to CMIP5. *Climate Dynamics*, 42(7):1999–2018.

Cai, W., Ng, B., Geng, T., Jia, F., Wu, L., Wang, G., Liu, Y., Gan, B., Yang, K., Santoso, A., Lin, X., Li, Z., Liu, Y., Yang, Y., Jin, F.-F., Collins, M., and McPhaden, M. J. (2023). Anthropogenic impacts on twentieth-century ENSO variability changes. *Nature Reviews Earth & Environment*, 4(6):407–418.

Cai, W., Santoso, A., Wang, G., Yeh, S.-W., An, S.-I., Cobb, K. M., Collins, M., Guilyardi, E., Jin, F.-F., Kug, J.-S., Lengaigne, M., McPhaden, M. J., Takahashi, K., Timmermann, A., Vecchi, G., Watanabe, M., and Wu, L. (2015). ENSO and greenhouse warming. *Nature Climate Change*, 5(9):849–859.

Callahan, C. W. and Mankin, J. S. (2023). Persistent effect of El Niño on global economic growth. *Science*, 380(6649):1064–1069.

Chan, D., Chan, S. C., Siddons, J. T., Cable, A., Faulkner, A., Cornes, R. C., Kent, E. C., Gebbie, G., and Huybers, P. (2026). DCENT-I: A Globally Infilled Extension of the Dynamically Consistent ENsemble of Temperature Dataset. *Geoscience Data Journal*, 13(2):e70054. _eprint: https://rmets.onlinelibrary.wiley.com/doi/pdf/10.1002/gdj3.70054.

Chan, D., Gebbie, G., and Huybers, P. (2025). Re-Evaluating Historical Sea Surface Temperature Data Sets: Insights From the Diurnal Cycle, Coral Proxy Data, and Radiative Forcing. *Geophysical Research Letters*, 52(13):e2025GL116615. _eprint: https://agupubs.onlinelibrary.wiley.com/doi/pdf/10.1029/2025GL116615.

Chung, C. T. Y., Power, S. B., Boschat, G., Gillett, Z. E., and Narsey, S. (2024). Projected Changes to Characteristics of El Niño-Southern Oscillation, Indian Ocean Dipole, and Southern Annular Mode Events in the CMIP6 Models. *Earth's Future*, 12(11):e2024EF005166.

Coles, S. (2001). *An Introduction to Statistical Modeling of Extreme Values*. Springer Series in Statistics. Springer London, London.

Diffenbaugh, N. S., Singh, D., Mankin, J. S., Horton, D. E., Swain, D. L., Touma, D., Charland, A., Liu, Y., Haugen, M., Tsiang, M., and Rajaratnam, B. (2017). Quantifying the influence of global warming on unprecedented extreme climate events. *Proceedings of the National Academy of Sciences*, 114(19):4881–4886.

Ehsan, M. A., L'Heureux, M. L., Tippett, M. K., Robertson, A. W., and Turmelle, J. (2024). Real-time ENSO forecast skill evaluated over the last two decades, with focus on the onset of ENSO events. *npj Climate and Atmospheric Science*, 7(1):301.

Eyring, V., Bony, S., Meehl, G. A., Senior, C. A., Stevens, B., Stouffer, R. J., and Taylor, K. E. (2016). GMD - Overview of the Coupled Model Intercomparison Project Phase 6 (CMIP6) experimental design and organization.

Freund, M. B., Henley, B. J., Karoly, D. J., McGregor, H. V., Abram, N. J., and Dommenget, D. (2019). Higher frequency of Central Pacific El Niño events in recent decades relative to past centuries. *Nature Geoscience*, 12(6):450–455.

Herring, S. C., Christidis, N., Hoell, A., Kossin, J. P., Schreck, C. J., and Stott, P. A. (2018). Explaining Extreme Events of 2016 from a Climate Perspective.

Huang, B., Thorne, P. W., Banzon, V. F., Boyer, T., Chepurin, G., Lawrimore, J. H., Menne, M. J., Smith, T. M., Vose, R. S., and Zhang, H.-M. (2017). Extended Reconstructed Sea Surface Temperature, Version 5 (ERSSTv5): Upgrades, Validations, and Intercomparisons.

Ishii, M., Nishimura, A., Yasui, S., and Hirahara, S. (2025). Historical High-Resolution Daily SST Analysis (COBE-SST3) with Consistency to Monthly Land Surface Air Temperature. *Journal of the Meteorological Society of Japan. Ser. II*, 103(1):17–44.

Izumo, T., Vialard, J., Lengaigne, M., and Suresh, I. (2020). Relevance of Relative Sea Surface Temperature for Tropical Rainfall Interannual Variability. *Geophysical Research Letters*, 47(3):e2019GL086182. _eprint: https://agupubs.onlinelibrary.wiley.com/doi/pdf/10.1029/2019GL086182.

Jiang, N., Zhu, C., McPhaden, M. J., Hu, Z.-Z., Lian, T., Zhou, C., and Chen, D. (2025). Atypical warming pattern of strong 2023-24 El Niño boosts global temperatures to new 1.5 °C record. *Communications Earth & Environment*, 6(1):1012.

Johnson, N. C. and Xie, S.-P. (2010). Changes in the sea surface temperature threshold for tropical convection. *Nature Geoscience*, 3(12):842–845.

Kennedy, J. J., Rayner, N. A., Atkinson, C. P., and Killick, R. E. (2019). An Ensemble Data Set of Sea Surface Temperature Change From 1850: The Met Office Hadley Centre HadSST.4.0.0.0 Data Set. *Journal of Geophysical Research: Atmospheres*, 124(14):7719–7763. _eprint: https://agupubs.onlinelibrary.wiley.com/doi/pdf/10.1029/2018JD029867.

Kirchmeier-Young, M. C., Gillett, N. P., Zwiers, F. W., Cannon, A. J., and Anslow, F. S. (2019). Attribution of the Influence of Human-Induced Climate Change on an Extreme Fire Season. *Earth's Future*, 7(1):2–10. _eprint: https://agupubs.onlinelibrary.wiley.com/doi/pdf/10.1029/2018EF001050.

Kirtman, B. P. (2016). Multi-Model ENSO Predictability in the NMME. volume 2016, pages A34E–02. ADS Bibcode: 2016AGUFM.A34E..02K.

Kumar, A., Chen, M., Xue, Y., and Behringer, D. (2015). An Analysis of the Temporal Evolution of ENSO Prediction Skill in the Context of the Equatorial Pacific Ocean Observing System.

Künsch, H. R. (1989). The Jackknife and the Bootstrap for General Stationary Observations. *The Annals of Statistics*, 17(3):1217–1241.

Lee, S., L'Heureux, M., Wittenberg, A. T., Seager, R., O'Gorman, P. A., and Johnson, N. C. (2022). On the future zonal contrasts of equatorial Pacific climate: Perspectives from Observations, Simulations, and Theories. *npj Climate and Atmospheric Science*, 5(1):82.

Liu, S., Dong, L., Song, F., McPhaden, M. J., and Wu, L. (2026). ENSO's Strengthened Control over Global Climate Anomalies in a Warmer World.

Liu, Y., Cai, W., Lin, X., Li, Z., and Zhang, Y. (2023). Nonlinear El Niño impacts on the global economy under climate change. *Nature Communications*, 14(1):5887.

Luhn, A. (2026). This El Niño will be the hottest by a huge margin.

L'Heureux, M. L., Harnos, D. S., Becker, E., Brettschneider, B., Chen, M., Johnson, N. C., Kumar, A., and Tippett, M. K. (2024a). How Well Do Seasonal Climate Anomalies Match Expected El Niño–Southern Oscillation (ENSO) Impacts?

L'Heureux, M. L., Tippett, M. K., Wheeler, M. C., Nguyen, H., Narsey, S., Johnson, N., Hu, Z.-Z., Watkins, A. B., Lucas, C., Ganter, C., Becker, E., Wang, W., and Liberto, T. D. (2024b). A Relative Sea Surface Temperature Index for Classifying ENSO Events in a Changing Climate.

Maher, N., Wills, R. C. J., DiNezio, P., Klavans, J., Milinski, S., Sanchez, S. C., Stevenson, S., Stuecker, M. F., and Wu, X. (2023). The future of the El Niño–Southern Oscillation: using large ensembles to illuminate time-varying responses and inter-model differences.

McPhaden, M. J., Zebiak, S. E., and Glantz, M. H. (2006). ENSO as an Integrating Concept in Earth Science. *Science*, 314(5806):1740–1745.

Moss, R. H., Edmonds, J. A., Hibbard, K. A., Manning, M. R., Rose, S. K., van Vuuren, D. P., Carter, T. R., Emori, S., Kainuma, M., Kram, T., Meehl, G. A., Mitchell, J. F. B., Nakicenovic, N., Riahi, K., Smith, S. J., Stouffer, R. J., Thomson, A. M., Weyant, J. P., and Wilbanks, T. J. (2010). The next generation of scenarios for climate change research and assessment. *Nature*, 463(7282):747–756.

Otto, F. E. L., Barnes, C., Philip, S., Kew, S., van Oldenborgh, G. J., and Vautard, R. (2024). Formally combining different lines of evidence in extreme-event attribution.

Philip, S., Kew, S., van Oldenborgh, G. J., Otto, F., Vautard, R., van der Wiel, K., King, A., Lott, F., Arrighi, J., Singh, R., and van Aalst, M. (2020). A protocol for probabilistic extreme event attribution analyses. *Advances in Statistical Climatology, Meteorology and Oceanography*, 6(2):177–203.

Planton, Y. Y., Guilyardi, E., Wittenberg, A. T., Lee, J., Gleckler, P. J., Bayr, T., McGregor, S., McPhaden, M. J., Power, S., Roehrig, R., Vialard, J., and Voldoire, A. (2021). Evaluating Climate Models with the CLIVAR 2020 ENSO Metrics Package.

Politis, D. N. and Romano, J. P. (1994). The Stationary Bootstrap. *Journal of the American Statistical Association*, 89(428):1303–1313.

Raghuraman, S. P., Soden, B., Clement, A., Vecchi, G., Menemenlis, S., and Yang, W. (2024). The 2023 global warming spike was driven by the El Niño–Southern Oscillation. *Atmospheric Chemistry and Physics*, 24(19):11275–11283.

Rayner, N. A., Parker, D. E., Horton, E. B., Folland, C. K., Alexander, L. V., Rowell, D. P., Kent, E. C., and Kaplan, A. (2003). Global analyses of sea surface temperature, sea ice, and night marine air temperature since the late nineteenth century. *Journal of Geophysical Research: Atmospheres*, 108(D14). _eprint: https://agupubs.onlinelibrary.wiley.com/doi/pdf/10.1029/2002JD002670.

Readfearn, G., Environment, G. R., and correspondent, c. (2026). 'We are waiting with bated breath': experts alarmed as BoM says gathering El Niño could be strongest on record. *The Guardian*.

Stott, P. A., Christidis, N., Otto, F. E. L., Sun, Y., Vanderlinden, J.-P., van Oldenborgh, G. J., Vautard, R., von Storch, H., Walton, P., Yiou, P., and Zwiers, F. W. (2016). Attribution of extreme weather and climate-related events. *WIREs Climate Change*, 7(1):23–41. _eprint: https://wires.onlinelibrary.wiley.com/doi/pdf/10.1002/wcc.380.

Taylor, K. E., Stouffer, R. J., and Meehl, G. A. (2012). An Overview of CMIP5 and the Experiment Design.

Tebaldi, C., Debeire, K., Eyring, V., Fischer, E., Fyfe, J., Friedlingstein, P., Knutti, R., Lowe, J., O'Neill, B., Sanderson, B., van Vuuren, D., Riahi, K., Meinshausen, M., Nicholls, Z., Tokarska, K. B., Hurtt, G., Kriegler, E., Lamarque, J.-F., Meehl, G., Moss, R., Bauer, S. E., Boucher, O., Brovkin, V., Byun, Y.-H., Dix, M., Gualdi, S., Guo, H., John, J. G., Kharin, S., Kim, Y., Koshiro, T., Ma, L., Olivié, D., Panickal, S., Qiao, F., Rong, X., Rosenbloom, N., Schupfner, M., Séférian, R., Sellar, A., Semmler, T., Shi, X., Song, Z., Steger, C., Stouffer, R., Swart, N., Tachiiri, K., Tang, Q., Tatebe, H., Voldoire, A., Volodin, E., Wyser, K., Xin, X., Yang, S., Yu, Y., and Ziehn, T. (2021). Climate model projections from the Scenario Model Intercomparison Project (ScenarioMIP) of CMIP6.

Tippett, M. K., Ranganathan, M., L'Heureux, M., Barnston, A. G., and DelSole, T. (2017). Assessing probabilistic predictions of ENSO phase and intensity from the North American Multimodel Ensemble. *Climate Dynamics*, 53(12):7497–7518.

van Oldenborgh, G. J., Hendon, H., Stockdale, T., L'Heureux, M., Coughlan de Perez, E., Singh, R., and van Aalst, M. (2021a). Defining El Niño indices in a warming climate. *Environmental Research Letters*, 16(4):044003.

van Oldenborgh, G. J., van der Wiel, K., Kew, S., Philip, S., Otto, F., Vautard, R., King, A., Lott, F., Arrighi, J., Singh, R., and van Aalst, M. (2021b). Pathways and pitfalls in extreme event attribution. *Climatic Change*, 166(1):13.

Watanabe, M., Kang, S. M., Collins, M., Hwang, Y.-T., McGregor, S., and Stuecker, M. F. (2024). Possible shift in controls of the tropical Pacific surface warming pattern. *Nature*, 630(8016):315–324.

Wheeler, M. C., Nguyen, H., Lucas, C., Chua, Z.-W., Grainger, S., Jones, D. A., L'Heureux, M. L., Noll, B., Meyers, T., Fauchereau, N. C., Peltier, A., Turkington, T., Kim, H.-J., and Umeda, T. (2024). Making Progress on the Operational Alerting of El Niño and La Niña in a Warming World.

Winters, J. (2026). El Niño is here, and it's already scrambling fisheries throughout the Pacific.

Yeh, S.-W., Cai, W., Min, S.-K., McPhaden, M. J., Dommenget, D., Dewitte, B., Collins, M., Ashok, K., An, S.-I., Yim, B.-Y., and Kug, J.-S. (2018). ENSO Atmospheric Teleconnections and Their Response to Greenhouse Gas Forcing. *Reviews of Geophysics*, 56(1):185–206. _eprint: https://agupubs.onlinelibrary.wiley.com/doi/pdf/10.1002/2017RG000568.

Climate change has intensified exceptional El Niño events like the 2026/27 forecast

Supplementary Material

Aditya Sengupta[1,2], Mandy B. Freund[1,2] ,and Andrew D. King[1,2]

[1] *School of Geography, Earth and Atmospheric Sciences, University of Melbourne, Melbourne, Kulin nations, Australia*

[2] *ARC Centre of Excellence for Weather of the 21st Century, Australia*

Supplementary Figures

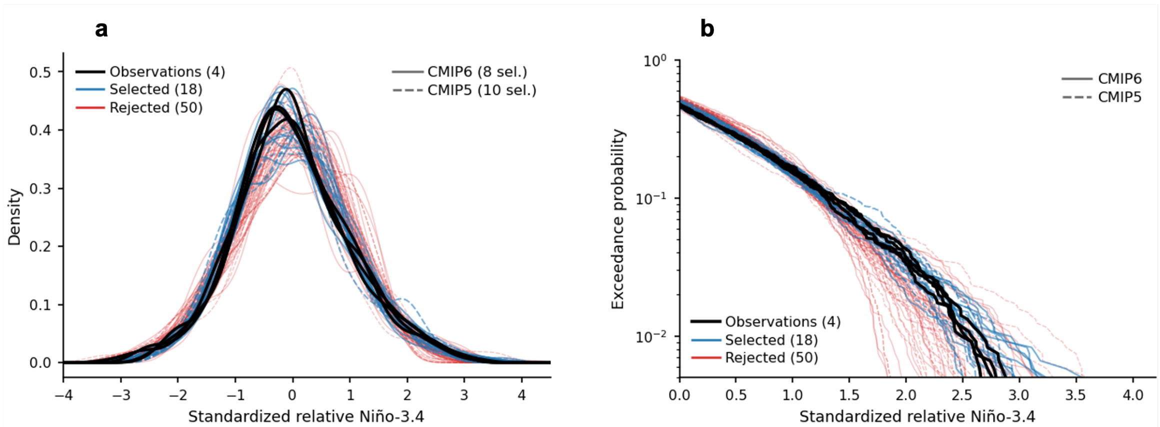

Figure S1. Evaluation of simulated relative Niño3.4 variability against observations. **a**, Kernel density estimates of standardised RONI over 1900–2000 for the four infilled observational analyses (black), the 18 models retained after evaluation (blue) and the 50 models rejected (red). Solid and dashed lines denote CMIP6 and CMIP5 models respectively. Series are standardised so that distributions are compared by shape rather than amplitude. **b**, Upper-tail exceedance probability for the same series, showing the frequency with which standardised RONI exceeds a given value.

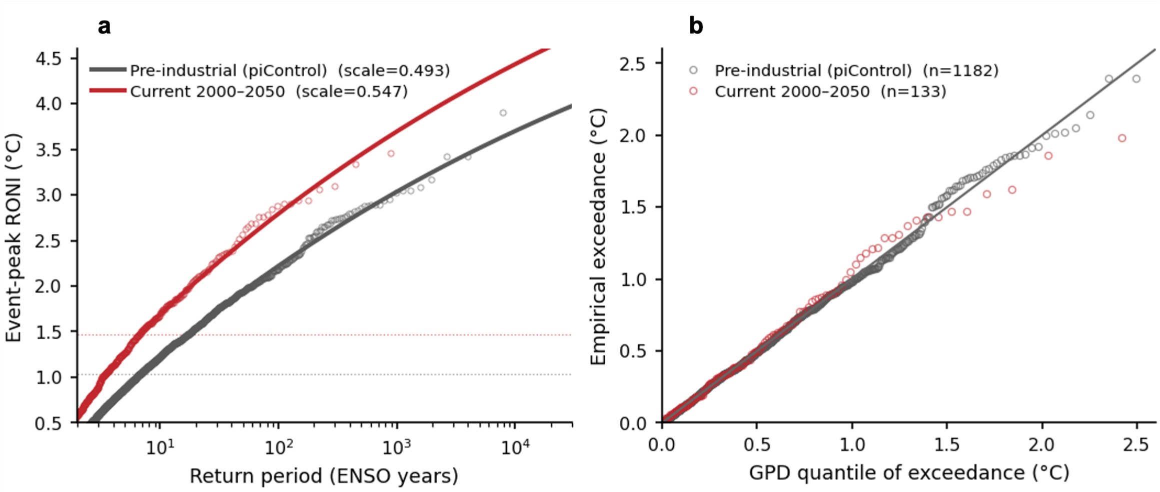

Figure S2. Diagnostics for the common-shape generalised Pareto fits. **a**, Return levels of annual peak RONI in the pre-industrial (grey) and current (red) climates. Open circles show empirical annual maxima and solid lines show the fitted GPD, drawn only above the 85th-percentile threshold used in the fit; dotted horizontal lines mark these thresholds. **b**, Quantile–quantile plot comparing empirical exceedances above the threshold with the corresponding GPD quantiles, for both climates. The one-to-one line indicates a perfect fit.

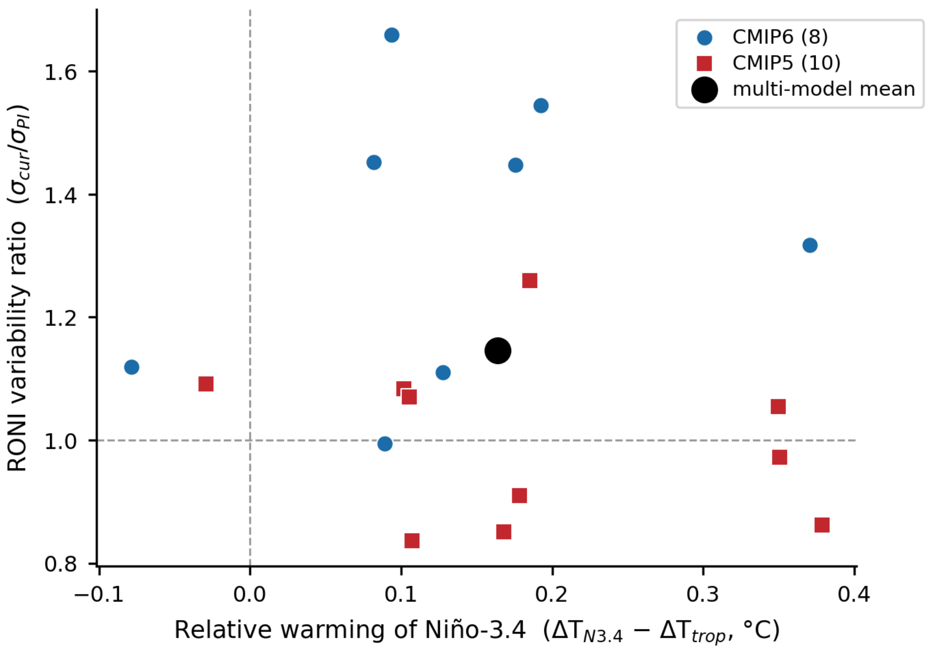

Figure S3. Contributions of mean-state change and variability change to the simulated shift in RONI. Each marker shows one evaluated model, comparing the relative warming of the Niño3.4 region (the difference between Niño3.4 and tropical-mean warming from piControl to 2000–2050) against the ratio of RONI standard deviation between the two periods. Circles denote CMIP6 models and squares CMIP5 models; the black marker shows the multimodel mean. Dashed lines represent zero relative warming and unchanged variability. Models in the upper-right quadrant simulate both an El Niño-like mean-state shift and increased ENSO variability.

Table S1. Models retained after evaluation. The 18 models whose relative Niño3.4 skewness over 1900–2000 falls within the observational reference range [+0.18, +0.44]. The amplitude factor is the ratio of observed to simulated ENSO standard deviation over 1900–2000, applied to all experiments of that model. ΔT_{rel} is the difference between Niño3.4 and tropical-mean warming from piControl to 2000–2050, and $\sigma_{\mathrm{cur}}/\sigma_{\mathrm{PI}}$ is the corresponding ratio of RONI standard deviations.

Model	Generation	Skewness	Amplitude factor	Sample size (years) piControl	Sample size (years) Current	ΔT_{rel} (°C)	$\sigma_{\mathrm{cur}}/\sigma_{\mathrm{PI}}$
CNRM-CM5	CMIP5	0.195	1.04	849	50	+0.102	1.084
GISS-E2-R	CMIP5	0.198	1.72	848	50	+0.379	0.862
MIROC-ESM-CHEM	CMIP5	0.207	2.34	254	50	+0.168	0.851
MIROC-ESM	CMIP5	0.237	2.47	629	50	+0.351	0.972
bcc-csm1-1-m	CMIP5	0.245	0.73	399	50	+0.350	1.055
CMCC-CM	CMIP5	0.273	1.47	329	50	−0.029	1.091
IPSL-CM5A-MR	CMIP5	0.303	1.26	299	50	+0.179	0.910
MIROC4h	CMIP5	0.385	1.42	99	35	+0.185	1.259
GFDL-ESM2M	CMIP5	0.410	0.64	499	50	+0.105	1.070
CCSM4	CMIP5	0.427	0.87	1050	50	+0.107	0.836
CESM2-WACCM	CMIP6	0.192	0.81	498	50	+0.176	1.448
MPI-ESM1-2-LR	CMIP6	0.192	1.33	999	50	+0.089	0.994
MRI-ESM2-0	CMIP6	0.256	0.93	700	50	+0.127	1.110
EC-Earth3-Veg-LR	CMIP6	0.314	1.22	500	50	+0.082	1.452
NESM3	CMIP6	0.357	1.41	499	50	−0.079	1.120
FIO-ESM-2-0	CMIP6	0.377	1.00	499	50	+0.370	1.317
MIROC6	CMIP6	0.416	0.99	799	50	+0.094	1.659
EC-Earth3	CMIP6	0.424	1.32	500	50	+0.193	1.544

Table S2. Attribution of the 2026/27 forecast El Niño event. Return periods, probability ratio and intensity change for the 2026/27 forecast, computed from a common-shape generalised Pareto fit ($q = 0.85$) to central estimate of the forecast annual peak RONI. The pre-industrial climate is represented by piControl (7,875 ENSO years) and the current climate by 2000–2050 of the concatenated historical and RCP4.5/SSP2-4.5 runs (885 ENSO years), pooled across 18 evaluated models. The fitted shape parameter is -0.087, with scale parameters of 0.493 (pre-industrial, $n = 1{,}182$ exceedances) and 0.547 (current, $n = 133$), giving a scale ratio of 1.109. Ranges are 5th–95th percentiles from a bootstrap resampling whole models with replacement over 1000 iterations.

	Magnitude	Return period (yr)		Probability ratio		Intensity
Event	(°C)	Pre-industrial	Current	Central	5–95%	change (°C)
2026/27 (forecast)	3.16	1497	242	6.2	3.1–15.2	+0.61

Table S3. Sensitivity of the probability ratio to analytical choices. Probability ratios for the forecast 2026/27 magnitude (3.16 °C) under alternative fitting procedures and model subsets. Ranges are 5th–95th percentiles from the model bootstrap.

Analysis	Probability ratio	Range
Main analysis (common-shape GPD, $q = 0.85$)	6.2	3.1–15.2
GPD threshold $q = 0.75$	7.7	4.0–16.5
GPD threshold $q = 0.80$	7.6	3.7–16.8
GPD threshold $q = 0.90$	6.1	2.6–15.1
Independently fitted shape parameters	4.2	1.3–12.9
GEV fitted to block maxima	17.3	5.2–87.1
CMIP6 models only ($n = 8$)	6.4	3.6–14.5
CMIP5 models only ($n = 10$)	5.0	0.4–44.4
Excluding MIROC-ESM variants ($n = 16$)	5.1	2.8–12.9

Table S4. Trends in relative Niño3.4 SST in observations and models. Linear trends in the annual-mean difference between Niño3.4 and ocean-masked tropical-mean SST, in °C per century. Positive values indicate that the Niño3.4 region has warmed faster than the tropical mean. Model values are from the concatenated historical and scenario runs of the 18 evaluated models, using a single realisation per model. Asterisks denote trends significant at the 5% level.

	1900–2025	1950–2025	1980–2025
Observations			
COBE-SST	−0.52*	−0.61*	−1.38*
DCSST-I	−0.13	−0.06	−0.92
HadISST	−0.50*	−0.55*	−1.06
ERSSTv5	−0.30*	−0.53	−1.25*
Models ($n = 18$)			
Multi-model mean	+0.12	+0.15	+0.15
Range across models	−0.16 to +0.31	−0.18 to +0.49	−0.74 to +0.50
Models with positive trend	16 of 18	13 of 18	13 of 18
Models with significant positive trend	3	2	0